

# Stretchable Microwave Transmission Lines Using Liquid-Metal Embedded Elastomers

Alexander M. Watson, Michael J. Ford, Eric J. Markvicka, William W. L. Fong, Suresh Venkatesh, Kaushik Sengupta, Carmel Majidi, and Christopher E. Tabor\*

The characterization of an RF transmitter composed of insulating and conducting regions of liquid-metal embedded elastomer (LMEE) is presented along with in situ measurements of LMEE microstrip lines as they are subjected to local material strains up to 40%. The LMEE is comprised of microscale droplets of a gallium–indium alloy that is liquid at room temperature and suspended within a cured elastomer matrix of polydimethylsiloxane (PDMS). The liquid metal microparticles were initially electrically isolated, but applying mechanical loading caused the permanent formation of highly localized conductive traces. Bonding films of LMEE onto a PDMS dielectric layer resulted in a stretchable microstrip structure that is capable of radio frequency (RF) transmission. Scattering parameter (*S*-parameter) measurements for reflection and transmission are presented for these microstrip lines as the electrical length increased up to 19%. A customized clamp was utilized to isolate the mechanical strain on the material from the electrical connectors and allow for transmission line characterization under applied strain and dielectric characterization of the LMEE material was performed. The stretchable microstrip lines show remarkable consistency in transmission response at 0.5–5 GHz when mechanically loaded to 40% strain for 1000 loading cycles.

these types of devices has been to identify suitable conducting materials that reliably perform under mechanical loading and elastic deformation. Two common solutions have emerged to achieve the desired mechanical and electrical properties within a single material. The first approach is to utilize geometric controls such as thinning typically brittle films down to flexible dimensions or deterministically patterning traces into compliant shapes like serpentine lines.<sup>[1,5]</sup> These approaches allow traditional materials to support moderate strains without affecting electrical performance and can be used for both conductive materials such as gold as well as crystalline semiconductors.<sup>[1,6]</sup> A second generalized approach has been to utilize intrinsically stretchable materials such as conjugated polymers<sup>[7]</sup> or liquid conductors. One of the most prominent liquid conductors has been gallium alloys, such as eutectic gallium indium (EGaIn) and Galinstan<sup>TM</sup> (Ga 68.5%/In 21.5%/Sn 10.0%), which have been demonstrated numerous times

as extremely stretchable DC conductors,<sup>[3,8–11]</sup> and recently a few EGaIn-based materials have been included in studies for stretchable and flexible RF systems.<sup>[4,8,12–14]</sup> The fabrication of stretchable liquid-metal conductors often utilizes microfluidics to control where the fluidic conductor resides, either through loading the liquid metal into prefabricated channels,<sup>[12,15]</sup> or


## 1. Introduction

Over the next decade, society will require electronics with enhanced mechanical compliance and durability to support rapid advancements in wearable internet of things (IoT) and sensing technologies.<sup>[1–4]</sup> One of the biggest challenges in the push for

A. M. Watson  
Electrical and Computer Engineering Technology  
University of Dayton  
Dayton, OH 45469, USA

M. J. Ford, C. Majidi  
Mechanical Engineering  
Carnegie Mellon University  
Pittsburgh, PA 15213, USA

E. J. Markvicka, C. Majidi  
Soft Machines Lab Robotics Institute  
Carnegie Mellon University  
Pittsburgh, PA 15213, USA

 The ORCID identification number(s) for the author(s) of this article can be found under <https://doi.org/10.1002/adem.202200345>.

DOI: 10.1002/adem.202200345

E. J. Markvicka  
Mechanical & Materials Engineering  
University of Nebraska-Lincoln  
Lincoln, NE 68588, USA

W. W. L. Fong  
Naval Information Warfare Center  
Pearl City, HI 96782, USA

S. Venkatesh, K. Sengupta  
Electrical and Computer Engineering Department  
Princeton University  
Princeton, NJ 08540, USA

C. E. Tabor  
Materials and Manufacturing Directorate  
Air Force Research Laboratory  
Dayton, OH 45433, USA  
E-mail: christopher.tabor.1@us.af.mil

directly printing the metal onto an elastomeric substrate that is then encapsulated.<sup>[16]</sup> These techniques tend to be a bit messy with many processing steps.

A hybrid approach to generating conductive materials that are more easily processed is to create a composite whereby a soft elastomer matrix is embedded with conductive fillers like silver flakes,<sup>[17,18]</sup> or nanowires.<sup>[19–21]</sup> Unfortunately, for most composites, the rigid fillers lead to degraded mechanical properties on the composite, especially when it comes to soft and elastic materials. A variation on this hybrid approach is to generate a composite that utilizes intrinsically flexible conductors as the filler in an elastomer, such as the gallium-based metal alloys mentioned earlier. Since these alloys remain liquid at room temperature, they represent a natural fit as the conductive material given the strain tolerance of its liquid phase,<sup>[3,16]</sup> which doesn't modify the mechanical properties of the elastomer matrix. A typical liquid-metal embedded elastomer (LMEE) is comprised of liquid-metal microparticles suspended in a soft elastomer matrix, often polydimethylsiloxane (PDMS).<sup>[9,10,22–27]</sup> The isolated EGaIn particles within the polymer result in an electrically insulating composite when the emulsion is cured. However, a mechanical stimulus such as compression or shear load can cause these composites to form percolating networks of droplets in which the liquid-metal coalesces along contiguous conductive paths. Thus, conductive traces can be “sintered”<sup>[28]</sup> into the material with a mechanical stimulus, while areas that do not undergo this mechanical process remain dielectric.<sup>[21,24]</sup>

While these various approaches to enabling mechanically compliant electronics have generally resulted in numerous DC or low-frequency studies, there are only a handful of reports on compliant and stretchable RF materials.<sup>[12,14,18,19]</sup> A significant reason for the lack of stretchable RF materials is that high-frequency electronics are governed by the total electromagnetic field response of both the conductor and the surrounding dielectric. As such, the successful implementation of RF circuits relies on an understanding of these materials' properties and their precise arrangement to achieve matching impedance within an RF network. Furthermore, the integration of soft RF materials

with standard, rigid counterparts is not trivial, as a slight mechanical disturbance at their interface can result in unwanted reflections at the interface, which degrades impedance matching. While LMEEs have provided some of the most promising electromechanical results to date,<sup>[22,26–30]</sup> they never before have been explored as compliant and stretchable RF materials.

Herein, we report the fabrication, characterization, and use of an LMEE material for stretchable RF transmission lines. The performance of LMEEs was characterized in situ while under various mechanical strains by utilizing a custom clamp designed to ensure the material strain was isolated from the RF connectors. The transmission and reflection coefficients as well as the attenuation and phase response of the microstrip transmission lines are presented while subjecting a section of the transmission line to a strain of up to 40%, resulting in an increase of the transmission line electrical length by a total of 19%. The DC response over the same strain is also shown to provide additional insight into the effect that strain has on the percolated liquid-metal traces. Finally, the RF performance of these microstrip transmission lines is shown to remain consistent with up to 1,000 cycles of strain.

## 2. RF Characterization of LMEE

A stretchable RF microstrip transmission line using LMEE was designed with the structure shown in **Figure 1**. The LMEE was fabricated as previously reported.<sup>[22,25]</sup> Briefly, a PDMS prepolymer (Sylgard 184, Dow) was mixed with a 50% volume fraction of EGaIn using a planetary mixer, which separated the liquid metal into microparticles and homogeneously dispersed them throughout the liquid polymer. The particles are on the scale of tens of micrometers and remained electrically isolated within the polymer until mechanically sintered together to generate a conductive path. Sintering is accomplished by applying highly concentrated pressure ( $\approx 1$  MPa) to the composite using either a mechanical scribe or roller.

Referring to Figure 1a, the transmission line consists of a stack of three layers. The bottom layer is a  $\approx 500$   $\mu\text{m}$  thick film

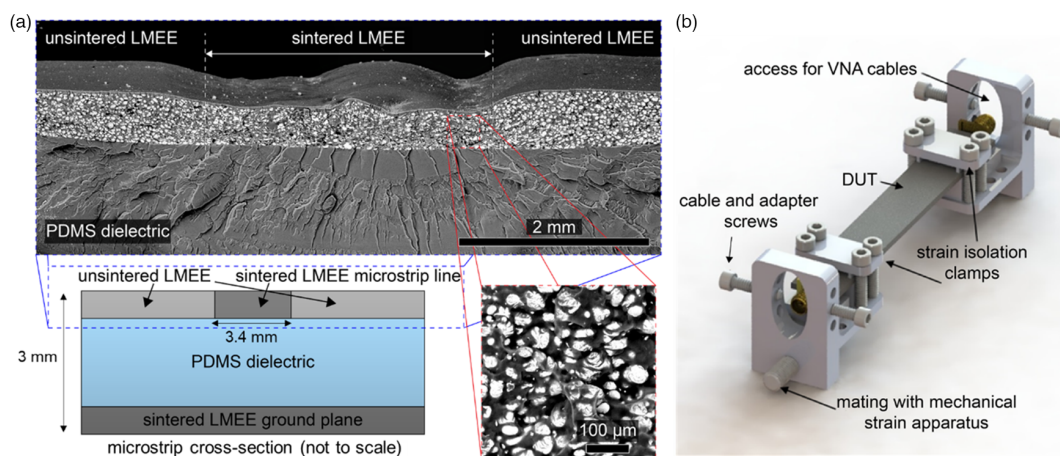


**Figure 1.** Illustration of liquid-metal embedded elastomer (LMEE) microstrip stack at various scales. a) Electron micrographs of the LMEE microstrip structure at various scales, depicting the top surface and cross-section. b) Rendering of the 3D-printed RF testing apparatus that allows the microstrip to undergo strain while isolating the strain from the RF connectors.

of LMEE that was fully sintered to generate a continuously conductive ground plane. The middle layer is a 2 mm thick slab of neat PDMS, which behaves as the dielectric layer without any liquid-metal microparticles present. The top layer is another film of LMEE material, with the dimensions of the microstrip line sintered down the middle of it. The three layers of the device were bonded by laminating them with a thin film of PDMS and curing the stack. The insets of Figure 1a show the configuration of the microstrip transmission line in cross-section, with multiple electron micrographs that depict representative examples of the microstrip at various scales. A schematic of the testing apparatus used to measure the strain-dependent RF transmission of the microstrip transmission line is shown in Figure 1b.

To determine the appropriate width of the sintered microstrip transmission line (for targeting an impedance match with the RF testing network at 50  $\Omega$ ), the RF material properties of all the materials used were characterized to provide an accurate model. As can be seen in the schematics of Figure 1, two dielectric materials and one conductive material were used to build the transmission line. The conductivity of bulk EGaIn has been reported as  $3.4 \times 10^6 \text{ S m}^{-1}$ ,<sup>[3]</sup> and was assumed here as an upper bound on the maximum conductivity the trace could achieve when fully sintered. (Note that previous studies suggest that mechanically sintered LMEEs have a conductivity  $\approx 10^4\text{--}10^5 \text{ S m}^{-1}$ .<sup>[22,25]</sup>) The dielectric that resides between the microstrip transmission line and the ground plane is pristine PDMS, while the second dielectric is the unsintered LMEE, located in the plane of the microstrip and containing isolated liquid-metal particles. The

dielectric constant and loss values of these dielectric materials were measured by casting and curing PDMS with various liquid-metal loadings into a rectangular X-band waveguide to obtain measurements from 8.2 to 12.4 GHz. This method minimized air gaps in the test fixture and led to high accuracy values without using an excessive amount of material (as compared to free space measurements). Using this technique, measurements of the LMEE were performed with a vector network analyzer (VNA) utilizing X-band waveguide launchers connected across the filled quarter-wave rectangular sample holders. Images of the X-band waveguides that were filled with PDMS of liquid-metal loadings from 0 to 50% are shown in Figure 2a.

The unsintered LMEE permittivity was measured and is shown in Figure 2b at a frequency of 8.2 GHz. The values are bounded by predictions obtained from the Maxwell–Garnett and Bruggeman effective medium theory models<sup>[31]</sup> (blue curve and yellow curve, respectively, in Figure 2b). These models serve to approximate a composite's effective permittivity with the inclusion of a uniform distribution of conductive spherical particles within a known dielectric. Such results are also consistent with measurements of permittivity as a function of LM volume fraction as previously reported.<sup>[23,32]</sup> However, in these studies, permittivity was only measured for relatively low frequencies in the range of 1 kHz–10 MHz. The effective permittivity of the LMEE material at high frequencies was utilized to determine the optimum geometry of a transmission line that was then fabricated to provide an impedance match to the RF network to deliver the maximum power through the transmission line.

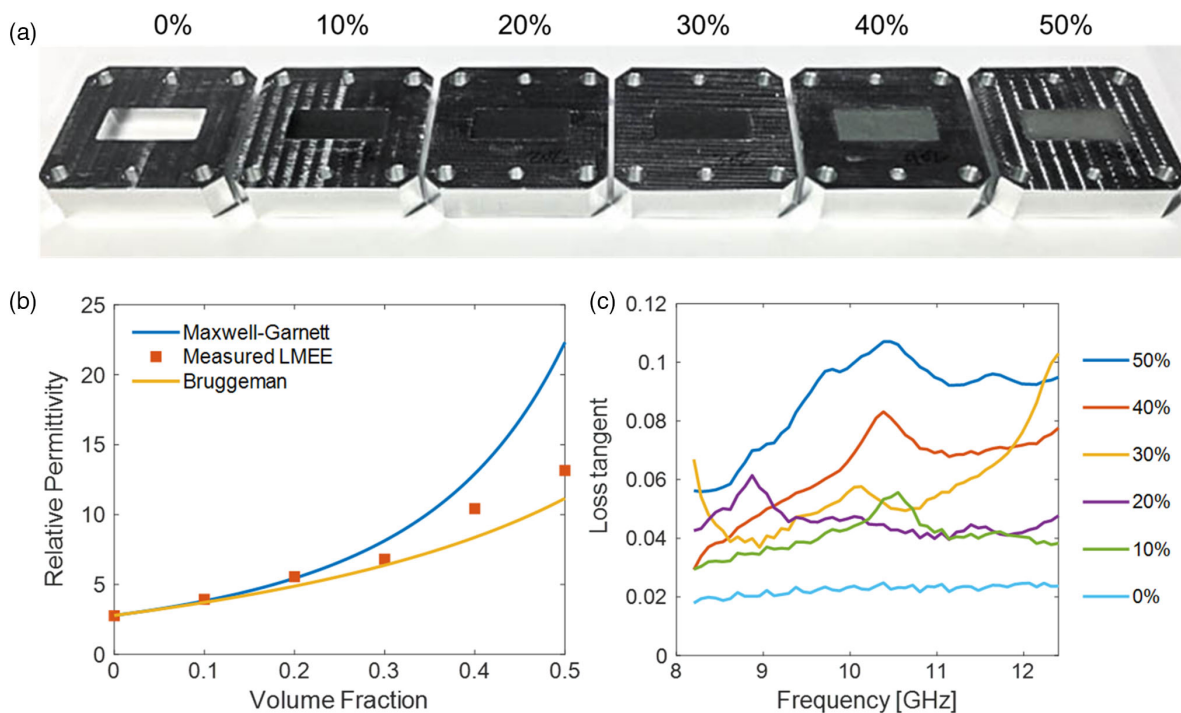


**Figure 2.** Dielectric measurements of LMEE for a range of volume fractions. a) Images of the various LMEE samples as cast into a quarter wavelength rectangular waveguide section for X-band material measurement. b) Measured values of the real permittivity for LMEE at 8.2 GHz compared to the Bruggeman and Maxwell–Garnett models for effective permittivity as a function of volume fraction of and inclusion of particles within a dielectric. Permittivity remained constant throughout the X-band. c) Measured loss tangent of the dielectric material over the X-band for different volume fraction percentages.

Figure 2c provides the frequency-dependent measurement of the loss tangent for the unsintered LMEE. An expected correlation exists between increased loss in the unsintered LMEE material as liquid metal is loaded at higher volume fractions; however, there is no strong quantitative corollary. Several spurious peaks arise in the loss tangent at various frequency bands for the different volume fractions. These peaks are likely due to specific microstructures within the unsintered films where particles randomly provide shape- and size-related loss characteristics. Regardless of the care taken to homogenize the unsintered LMEE, the dielectric loss is unpredictable at any one given frequency due to slight variations in particle size and shape between samples, accounting for the different peaks across frequency. This is acceptable, however, since the loss tangent value affects the transmission line efficiency but does not significantly affect the layout dimensions of the microstrip for impedance matching, and primarily serves to provide insight into the expected transmission loss due to the dielectric material. For example, the neat PDMS (0% liquid metal) with a flat loss tangent of 0.02 across frequency would add an attenuation loss on the transmission line of  $0.0015 \text{ dB mm}^{-1}$  at 0.5 GHz, and  $0.013 \text{ dB mm}^{-1}$  at 4.5 GHz, from standard transmission line theory.<sup>[33]</sup> This dielectric loss is only one part of the total attenuation of the transmission line, and the full attenuation parameter is discussed in the next section.

The volume fraction of 50% was selected for the microstrip, as it provided the most consistent conductive trace after undergoing mechanical sintering while retaining the elastic properties of the PDMS host. The previous characterization of this material highlights electromechanical properties such as modulus and low-frequency dielectric properties.<sup>[23]</sup> Composites with higher volume fractions of EGaIn have been reported by using a combination of shear mixing and sonication,<sup>[32]</sup> but higher loading also increases the relative permittivity, which would shrink the dimensions required to achieve a  $50 \Omega$  characteristic impedance microstrip, making accurate fabrication more difficult. By knowing the PDMS and LMEE permittivity, a  $50 \Omega$  transmission line with a trace width of 3.4 mm was modeled to match the VNA impedance and minimize unwanted reflections. This modeling was done using methods for analyzing multilayer microstrip structures,<sup>[34]</sup> and standard microstrip transmission line equations,<sup>[35]</sup> with further elaboration detailed in the Supporting Information.

### 3. In Situ Testing of LMEE Microstrip Transmission Line

To evaluate the device under test (DUT), a VNA was used to measure the RF response of the transmission line as it undergoes strain. The designed microstrip device was connected on both sides to coaxial RF cables terminating in Subminiature Version A (SMA) connectors and affixed by the connector fixtures that were fabricated in-house (Figure 1b). The use of this fixture was critical because any unsecured connection to the stretchable LMEE material could cause severe sensitivity to any physical movement, resulting in completely undiscernible and unreliable measurements. The test fixture was built to secure the interface between the soft LMEE and rigid SMA connector, preventing any strain on the DUT from affecting this connection.

The custom clamping mechanism is shown in Figure 1b and is elaborated on in the Figure S1, Supporting Information. By using this fixture to secure the RF cables to the soft LMEE substrate, characterization of the DUT was performed in situ while the device was strained, providing a response of the transmission line that is independent of the sensitive coaxial/microstrip connection.

Several LMEE microstrip devices were fabricated to study how the material behaves as an RF transmission line. Each sample was secured into the testing apparatus as previously described and in the Supporting Information (Figure S1). The VNA coaxial cables were then secured to the adapters with sufficient torque to avoid slipping, and the entire connection assembly from coaxial VNA cable to SMA adapter to LMEE was secured in the testing apparatus with set screws. Each end of the secured microstrip was then mounted onto the mechanical stretching system that applies strain on the DUT by varying the distance between the two secured ends. The VNA was calibrated to include the cables, thereby setting the measurement reference plane to the end of the coaxial cable. In this way, all measurements include the SMA connection to the DUT as part of the data, and therefore the response of the connection between rigid and soft materials is captured, which can be used to qualify the effectiveness and importance of proper care in the mating between these disparate material sets.

#### 3.1. Strain Response on S-Parameters

The S-parameters collected by the VNA while the LMEE was under local elongation strains of 0%, 20%, and 40% are shown in Figure 3. It is important to note that while using the test apparatus to create these local strains of 20% and 40% on the middle section of the transmission line between the clamps, the overall electrical length between the VNA cables increases by a smaller percentage (5.2% and 10.4%, respectively) of the original electrical length. The S-parameters are depicted in log scale, and since the DUT is passive, all values are negative, indicating insertion loss and return loss in the transmission ( $S_{21}$ ) and reflection ( $S_{11}$ ) signal, respectively. As the microstrip length increases, two changes in these S-parameters would be expected to occur: 1) the transmission ratio should decrease as the longer line consumes more power, and 2) the peaks and valleys in the reflection ratio should shift to lower frequencies since the finite-length transmission line is becoming longer.

Figure 3a shows how the transmission ratio only slightly decreases as the electrical length increases. The reflection ratio depicted as the  $S_{11}$  in Figure 3b indicates a good impedance match, with reflections at all measured frequencies staying below a  $-10 \text{ dB}$  threshold. These reflections arise from slight discrepancies between the VNA cable impedance and the fabricated microstrip impedance. This slight mismatch is illustrated by several reflection peaks and valleys across the frequency range resulting from the interfaces between the calibrated VNA cables and the transmission line of finite length. These reflection peaks and valleys correspond to the integer multiples of quarter wavelengths that match the finite transmission line's length. As the microstrip electrical length increases, the reflection ratio remains near-constant value, but shifts these peaks and valleys to lower frequency. Importantly, the act of straining the sample does



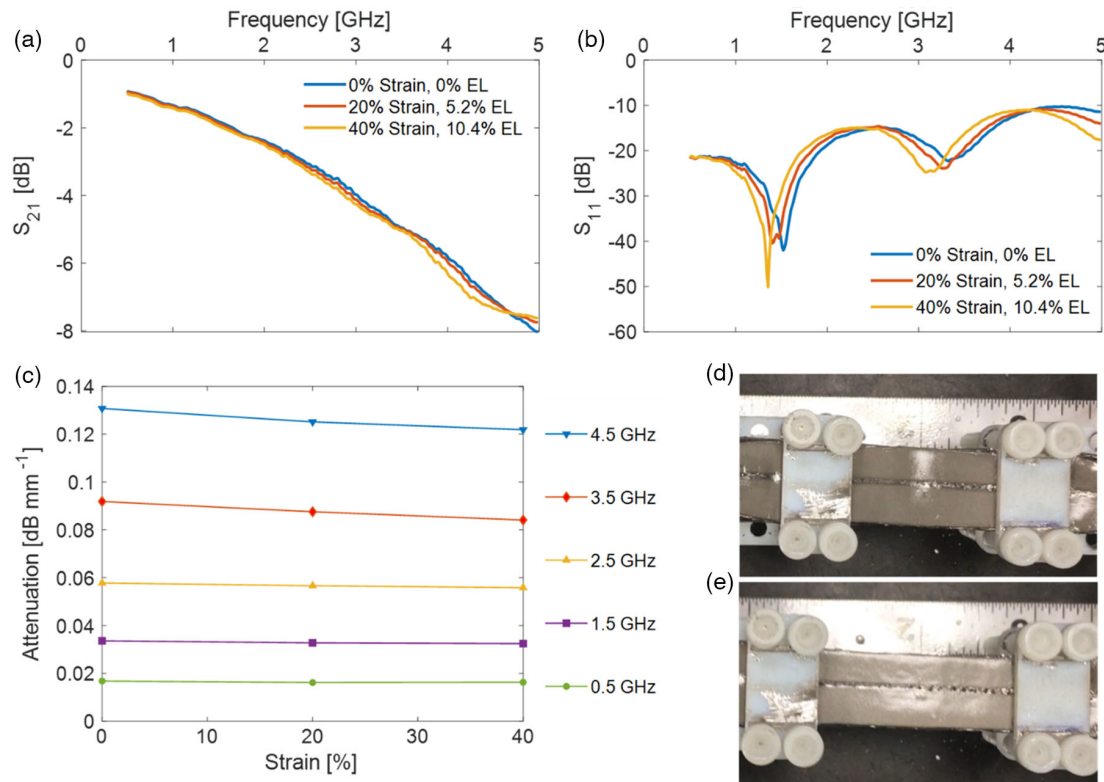


**Figure 3.** S-parameter measurements for an LMEE microstrip under strain. a)  $S_{21}$  transmission and b)  $S_{11}$  reflection through the microstrip as it strains by 20% (5.2% electrical length) and 40% (10.4% electrical length). c) Attenuation of the LMEE material over strain at various frequencies. d–e) Images of an LMEE device under test at 0% and 40% strain, respectively.

not affect the reflection ratio magnitude, indicating that the sensitive connection between SMA and LMEE microstrip is indeed secured and unaffected by the act of straining the DUT.

To evaluate the LMEE material's performance under strain and differentiate the loss expected from elongating the transmission line versus any additional loss incurred as a result of straining the material, an analysis of the material attenuation factor was performed. Taking the stretchable transmission line's  $S_{21}$  value and normalizing it by its length yields an attenuation constant for the LMEE material, depicting the loss per unit length. Figure 3c shows this attenuation constant in units of dB mm<sup>-1</sup> versus strain of the transmission line at various frequencies. This attenuation measurement represents all sources of loss, including dielectric loss, metal conductivity losses, leakage through the dielectric, and radiation. Of these losses, typically the dominant sources for microstrip transmission lines are the metal conductivity and the dielectric loss characterized by the loss tangent. From the loss tangent measurements of neat PDMS, which is the largest proportion of the microstrip stack and where the majority of the electric fields are located, we anticipate approximate values of 0.0015 dB mm<sup>-1</sup> at 0.5 GHz and 0.013 dB mm<sup>-1</sup> at 4.5 GHz, as mentioned in the previous section. Compared to the overall attenuation shown in Figure 3c, this suggests that the most dominant source of loss is the metal conductivity. Interestingly, the material's loss per length remains fairly constant even as the LMEE is stretched to 20% and 40% strain. Further analysis on the trace conductivity under strain is

explored in the next section, along with an analysis of the phase propagation. The loss of the LMEE material is higher than most standard RF materials, mostly due to the higher resistivity of the EGaIn (an order of magnitude higher than copper<sup>[3]</sup>), while the dielectric loss is similar to standard printed circuit board material. However, the change in the material performance as it is strained is nearly negligible, and therefore provides a unique stretchability in the RF transmission line that does not significantly alter the material's ability to transmit power.

### 3.2. Comparing Strain Effect on DC Conductivity and RF Transmission Delay

To further evaluate the effect strain has on the LMEE electrical performance, a collection of measurements for five microstrip transmission lines was taken and normalized to unstrained measurements of the DUT's performance. Recent work has reported that the normalized DC resistance of LMEEs is unaffected by strain.<sup>[10,11,22,25,26,36]</sup> This counterintuitive effect for particle-based conductors being insensitive to strain has been theorized to arise from the morphology of the percolated conductive trace yielding to macro-scale deformation of the composite while retaining the overall internal shape of the conductor. One example of such a trace is a connected network of LM droplets that form a horseshoe-like serpentine pathway, as illustrated in

Figure 4a, which has been recently studied.<sup>[27]</sup> This microstructure allows for stretching of the LMEE without elongating the conductive path, thereby retaining the trace's original resistance. The DC resistance of the LMEE transmission lines used herein was measured by connecting the top microstrip trace and the bottom ground plane in series, using an SMA electrical shorting cap on one side of the microstrip. Each resistance was normalized to its initial resistance at zero strain and plotted for comparison in Figure 4b, confirming previously reported strain invariant resistance values for these devices. We postulate that this explanation holds true for the material attenuation constant as reported in Figure 3c, leading to the remarkable phenomenon where the act of straining the material does not significantly affect the attenuation from conductor losses.

The attenuation constant is just one part of the total propagation constant that governs the electromagnetic field transmission through the material. While the attenuation constant affects the amplitude of the signal per unit length, the phase constant dictates the oscillations per unit length, and is linearly related to the signal frequency. An important feature of an ideal transmission line is that it has a linear phase shift (or constant group delay). This implies that the signals containing multiple frequencies do not suffer from distortion as they pass through the line, as each frequency component is delayed by the same amount of time. Phase measurements of the transmitted signals were analyzed to understand the delay to study how strain might affect the distortion.

To measure RF delay as a function of strain, the phase data from the  $S_{21}$  measurements was unwrapped to display the change in phase linearly with frequency, as expected for a transmission line. The group delay of the transmission line was determined by taking the slope of this phase data over frequency,

which can be found for the devices at various strains. To investigate how the strain affects the delay, each sample's strained group delay is normalized to its unstrained group delay and plotted as a function of its overall stretch, given as the transmission line's current length divided by its initial length. The results for a collection of measurements from five transmission lines are shown in Figure 4c. The group delay of transmitted power through the LMEE transmission lines is expected to depend linearly on the length of the transmission line assuming isotropic material properties and this linear profile is provided with the solid line. The measured changes in group delay correspond with the expected changes for an increasing transmission line length. This signifies that the act of straining the material does not significantly alter the phase velocity of the material, maintaining its phase constant. It should be noted that the measured phase data and therefore group delay includes the lengths of the SMAs on either side. In addition, due to the disparate material sets, accounting for the phase effects of these SMAs requires an evaluation of equivalent electrical lengths before the normalization. Further detail of the length normalization can be found in the Supporting Information.

Another final important characterization for stretchable conductors is their durability under cyclical mechanical loading. Figure 5 provides S-parameter measurements of an LMEE microstrip sample undergoing strain from 0 to 40% over 1,000 repeated cycles. The response of the LMEE microstrip is unchanged between cycles 1 and 1,000, demonstrating the durability of the material, once its initial morphology is established. The initial difference between the unstrained measurement (blue curves) and the subsequent measurements demonstrates that the first strain is likely important to establish an initial reorganized internal morphology of the sintered trace. Once this

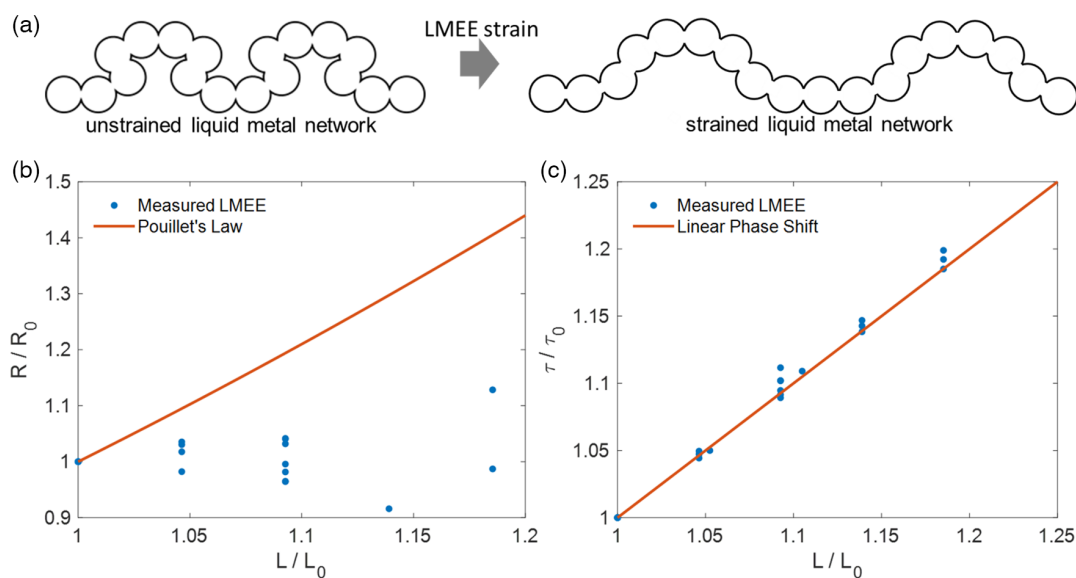


**Figure 4.** Normalized electrical responses under strain. a) Illustration of the horseshoe-like serpentine path<sup>[27]</sup> that yields macro-scale strain while retaining original conductive pathlength. b) DC resistance measurements of LMEE microstrip samples normalized to initial resistance measurements and plotted versus stretch as compared to expected response of elongating an incompressible conductive material according to Pouillet's Law and the Poisson Effect. c) Phase delay of LMEE microstrip samples normalized to initial phase delay measurements and plotted versus stretch as compared to the expected linear response of phase and transmission line length.

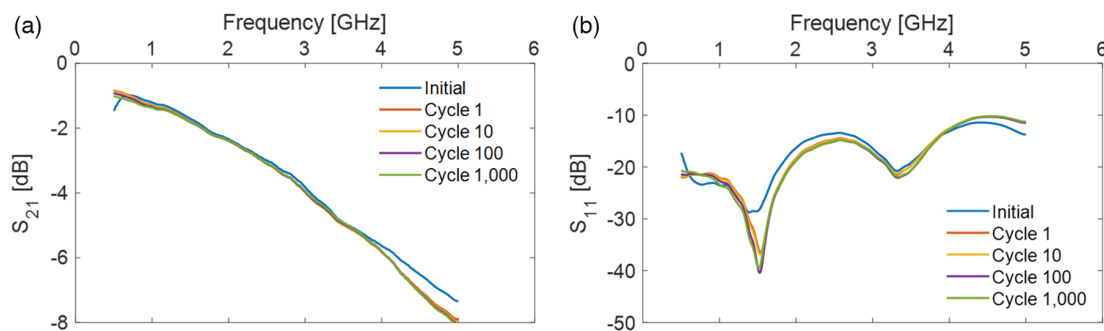


**Figure 5.** Cycling LMEE microstrip device under test (DUT) from 0% to 40% strain up to 1,000 cycles. a) Plot of  $S_{21}$  transmission response. b) Plot of the  $S_{11}$  reflection response. The most distinct change occurs during the initial strain cycle, while the next 1,000 cycles show minimal effect.

small relaxation occurs, the performance of the RF microstrip trace is exceptionally consistent over the cycles measured.

#### 4. Conclusion

The in situ RF characterization of microstrip transmission lines composed of LMEE was demonstrated. The response of this unique material set as a stretchable RF conductor was shown to undergo mechanical strain up to 40%. To model a 50  $\Omega$  matched transmission line, the dielectric properties of the LMEE dielectric (unsintered) were measured via casting the material directly into an RF waveguide. Using these material properties, an LMEE microstrip transmission line was fabricated and the effect of strain on the RF transmission was measured using a vector network analyzer to obtain  $S$ -parameters. DC measurements performed here and elsewhere demonstrate no change in the resistance of the LMEE line under strain, and this effect is demonstrated for the first time here in the RF when considering the near-constant RF attenuation factor, even as the DUT is strained up to 40%. This independence of RF attenuation performance over strain is attributed to the same 3D serpentine morphology of the conductive path within the LMEE that leads to the DC resistance insensitivity. The RF group delay increases linearly with the overall length of the transmission lines, as this delay depends on the propagation of the electromagnetic fields through the dielectric, which is bounded by the overall length of the entire microstrip rather than the percolated conductive path. Taken together, the constant attenuation and phase response of the material under strain provides a unique RF transmission line that remains distortionless while being stretched. The transmission lines provide a robust and consistent transmission response when cycled 1,000 times to local material strains of 40%. These results indicate that while the RF loss of the LMEE material may be larger than most other conductors, it functions well for localized areas of high strain where RF transmission is required, such as at the creases of foldable antennas or wearable electronics.

#### 5. Experimental Section

**LMEE Composite:** 75 wt% gallium and 25 wt% indium (EASCHEM) were alloyed by first melting gallium and then stirring in indium at elevated temperatures until completely mixed. EGaIn was mechanically sheared

into droplets by mixing with PDMS (Sylgard 184, Dow) precursors until mm-sized droplets of liquid metal were formed. The composite was prepared by mixing PDMS and EGaIn at loadings up to 50 vol%. PDMS was cured at a 10:1 oligomer/curing agent ratio. After initial mixing to form mm-sized droplets, microdroplets were formed using an AR-100 THINKY planetary centrifugal mixer (mixing: 1 min). After mixing, the viscous mixture was cast into the appropriate geometry using acrylic stencils. The composites were cured in an oven for >30 min. at 60–80 °C. A razor blade or ballpoint pen was used to apply a mechanical force to sinter the droplets into conductive traces. A thin polyethylene sheet was placed on the surface of the LMEE composite to prevent direct contact with the scribing tip. For sheets of PDMS, the 10:1 oligomer/curing agent ratio was also used. Separate sheets of PDMS and LMEE were laminated by using a thin layer of uncured PDMS as an adhesive and then curing.

**Microstrip Design:** The microstrip consists of a three-layer stack of LMEE, PDMS, and LMEE, where the bottom LMEE material is fully sintered to act as the ground plane, and the top LMEE was selectively sintered to create the microstrip transmission line. The microstrip dimensions were designed using equations for microstrip impedance from<sup>[33]</sup> and adapted to account for the multilayer stack that includes the 2 mm PDMS dielectric layer as well as the surrounding unsintered LMEE layer, using methods from<sup>[34]</sup>. The effective permittivity for this microstrip was calculated to be  $\epsilon_{\text{eff}} = 2.87$  and the resulting line width to attain a 50  $\Omega$  impedance match was 3.4 mm. Further elaboration on the methodology used for the design is contained in the Supporting Information. The total width of the LMEE microstrip was set to 14 mm to fit into the strain isolation clamp and mechanical stretching system.

**RF Measurement Methods:** The RF measurement of the transmission lines was performed using a Keysight E8362C PNA Microwave Network Analyzer with the stimulus set from 0.5 to 5 GHz. The network analyzer was connected using coaxial cables to SMA adapters, which have been modified to accommodate the LMEE microstrip stack. Copper shim was soldered onto the bottom ground pins of the SMA to fit the microstrip snug in between the SMA center pin on top, and the shimmed ground plane on the bottom. The microstrip was set onto the custom clamp as depicted in Figure 1a, and the SMA adapters were fit into place on either end. A schematic of this test setup and further details are provided in the Supporting Information. After a good electrical connection was made, the entire adapter and microstrip end were secured to the clamp apparatus with the set screws. Next, the strain isolation clamps were fitted onto the top of the LMEE microstrip and tightened to fix the material to the clamp underside. Finally, both ends of the clamp mount were affixed to the arms of a mechanical stretcher system (Admet eXpert 8000). A measurement between the clamped portions of the microstrip was made, and a final position on the stretcher controller software (MTEST Quattro) was set so that the material undergoes a maximum of 40% strain for this mechanically isolated section of the transmission line. Due to the various lengths of microstrips tested and the 40% strain limit set on the material, the total transmission line electrical lengths saw an increase up to 19%.

The mechanical stretcher strained the samples at a rate of 300 mm min<sup>-1</sup>, and would pause at various intervals to allow the VNA to capture the RF data in situ.

## Supporting Information

Supporting Information is available from the Wiley Online Library or from the author.

## Acknowledgements

The authors acknowledge funding for this work supported by a Multi-University Research Initiative (MURI) from the Air Force Office of Scientific Research under grant number FA9550-16-1-0566.

## Conflict of Interest

The authors declare no conflict of interest.

## Data Availability Statement

The data that support the findings of this study are available from the corresponding author upon reasonable request.

## Keywords

EGaIn, liquid-metal electronics, liquid-metal embedded elastomer, stretchable electronics, stretchable RF

Received: March 9, 2022

Published online:

- [1] J. A. Rogers, T. Someya, Y. Huang, *Science* **2010**, 327, 1603.
- [2] A. Nathan, A. Ahnood, M. T. Cole, S. Lee, Y. Suzuki, P. Hiralal, F. Bonaccorso, T. Hasan, L. Garcia-Gancedo, A. Dyadyusha, S. Haque, P. Andrew, S. Hofmann, J. Moultrie, D. Chu, A. J. Flewitt, A. C. Ferrari, M. J. Kelly, J. Robertson, G. A. J. Amaratunga, W. I. Milne, *Proc. IEEE* **2012**, 100, 1486.
- [3] M. D. Dickey, *Adv. Mater.* **2017**, 29, 1606425.
- [4] Z. Wu, K. Hjort, S. H. Jeong, *Proc. IEEE* **2015**, 103, 1211.
- [5] J. A. Fan, W.-H. Yeo, Y. Su, Y. Hattori, W. Lee, S.-Y. Jung, Y. Zhang, Z. Liu, H. Cheng, L. Falgout, M. Bajema, T. Coleman, D. Gregoire, R. J. Larsen, Y. Huang, J. A. Rogers, *Nat. Commun.* **2014**, 5, 1.
- [6] N. K. Mahenderkar, Q. Chen, Y.-C. Liu, A. R. Duchild, S. Hofheins, E. Chason, J. A. Switzer, *Science* **2017**, 355, 1203.
- [7] L. Kayser, D. Lipomi, *Adv. Mater.* **2019**, 31, 1806133.
- [8] S. H. Jeong, A. Hagman, K. Hjort, M. Jobs, J. Sundqvist, Z. Wu, *Lab. Chip* **2012**, 12, 4657.
- [9] N. Kazem, T. Hellebrekers, C. Majidi, *Adv. Mater.* **2017**, 29, 1605985.
- [10] M. J. Ford, C. P. Ambulo, T. A. Kent, E. J. Markvicka, C. Pan, J. Malen, T. H. Ware, C. Majidi, *Proc. Natl. Acad. Sci.* **2019**, 116, 21438.
- [11] C. J. Thrasher, Z. J. Farrell, N. J. Morris, C. L. Willey, C. E. Tabor, *Adv. Mater.* **2019**, 31, 1903864.
- [12] K. Entesari, A. P. Saghati, *IEEE Microwave Mag.* **2016**, 17, 50.
- [13] M. Rashed Khan, G. J. Hayes, J.-H. So, G. Lazzi, M. D. Dickey, *Appl. Phys. Lett.* **2011**, 99, 013501.
- [14] S. Cheng, Z. Wu, *Lab. Chip* **2010**, 10, 3227.
- [15] C. Koo, B. E. LeBlanc, M. Kelley, H. E. Fitzgerald, G. H. Huff, A. Han, *J. Microelectromech. Syst.* **2015**, 24, 1069.
- [16] K. Khoshmanesh, S.-Y. Tang, J. Y. Zhu, S. Schaefer, A. Mitchell, K. Kalantar-zadeh, M. D. Dickey, *Lab. Chip* **2017**, 17, 974.
- [17] J. Agar, J. Durden, D. Staiculescu, R. Zhang, E. Gebara, C. P. Wong, in *2011 IEEE MTT-S Int. Microw. Symp.*, Baltimore, MD, USA **2011**, p. 1.
- [18] F. Cai, Z. Li, J. C. Agar, C. P. Wong, J. Papapolymerou, in *2012 IEEE/MTT-S Int. Microw. Symp.*, Montreal, Quebec, Canada **2012**, pp. 1–3.
- [19] T. Rai, P. Dantes, B. Bahreyni, W. Soo Kim, *IEEE Electron Device Lett.* **2013**, 34, 544.
- [20] C. Wu, L. Fang, X. Huang, P. Jiang, *ACS Appl. Mater. Interfaces* **2014**, 6, 21026.
- [21] F. Xu, Y. Zhu, *Adv. Mater.* **2012**, 24, 5117.
- [22] A. Fassler, C. Majidi, *Adv. Mater.* **2015**, 27, 1928.
- [23] M. D. Bartlett, A. Fassler, N. Kazem, E. J. Markvicka, P. Mandal, C. Majidi, *Adv. Mater.* **2016**, 28, 3726.
- [24] M. D. Bartlett, N. Kazem, M. J. Powell-Palm, X. Huang, W. Sun, J. A. Malen, C. Majidi, *Proc. Natl. Acad. Sci.* **2017**, 114, p. 2143.
- [25] E. J. Markvicka, M. D. Bartlett, X. Huang, C. Majidi, *Nat. Mater.* **2018**, 17, 618.
- [26] N. Cohen, K. Bhattacharya, *Int. J. Non-Linear Mech.* **2019**, 108, 81.
- [27] N. Zolfaghari, P. Khandagale, M. J. Ford, K. Dayal, C. Majidi, *Soft Matter* **2020**.
- [28] J. W. Boley, E. L. White, R. K. Kramer, *Adv. Mater.* **2015**, 27, 2355.
- [29] L. Zhu, B. Wang, S. Handschuh-Wang, X. Zhou, *Small* **2020**, 16, 1630.
- [30] Y. Lin, J. Genzer, M. D. Dickey, *Adv. Sci.* **2020**, 7, 2198.
- [31] D. E. Aspnes, *Am. J. Phys.* **1982**, 50, 704.
- [32] R. Tutika, S. Kmiec, A. B. M. T. Haque, S. W. Martin, M. D. Bartlett, *ACS Appl. Mater. Interfaces* **2019**, 11, 17873.
- [33] D. Pozar, *Microwave Engineering*, Addison-Wesley, Reading, MA **1990**.
- [34] E. Yamashita, *IEEE Trans. Microw. Theory Tech.* **1968**, 16, 529.
- [35] B. Wadell, *Transmission Line Design Handbook*, Artech House, Boston, MA **1991**.
- [36] Z. Yu, J. Shang, X. Niu, Y. Liu, G. Liu, P. Dhanapal, Y. Zheng, H. Yang, Y. Wu, Y. Zhou, Y. Wang, D. Tang, R.-W. Li, *Adv. Electron. Mater.* **2018**, 4, 1800137.